Journal of
Synchrotron Radiation

ISSN 0909-0495

Received 6 February 2008
Accepted 29 March 2008

Differential phase contrast with a segmented detector in a scanning X-ray microprobe

B. Hornberger,[a]*‡ M. D. de Jonge,[b]¶ M. Feser,[a]‡ P. Holl,[c,d] C. Holzner,[a] C. Jacobsen,[a] D. Legnini,[b] D. Paterson,[b]¶ P. Rehak,[e] L. Strüder[f,d] and S. Vogt[b]

[a]Department of Physics and Astronomy, Stony Brook University, Stony Brook, NY 11794-3800, USA, [b]Advanced Photon Source, Argonne National Laboratory, Argonne, IL 60439-4856, USA, [c]PNSensor GmbH, Römerstr. 28, 80803 München, Germany, [d]MPI Halbleiterlabor, Otto-Hahn-Ring 6, 81739 München, Germany, [e]Instrumentation Division, Brookhaven National Laboratory, Upton, NY 11973, USA, and [f]Max-Planck-Institut für extraterrestrische Physik, 85741 Garching, Germany. E-mail: hornberg@xray1.physics.sunysb.edu

Scanning X-ray microprobes are unique tools for the nanoscale investigation of specimens from the life, environmental, materials and other fields of sciences. Typically they utilize absorption and fluorescence as contrast mechanisms. Phase contrast is a complementary technique that can provide strong contrast with reduced radiation dose for weakly absorbing structures in the multi-keV range. In this paper the development of a segmented charge-integrating silicon detector which provides simultaneous absorption and differential phase contrast is reported. The detector can be used together with a fluorescence detector for the simultaneous acquisition of transmission and fluorescence data. It can be used over a wide range of photon energies, photon rates and exposure times at third-generation synchrotron radiation sources, and is currently operating at two beamlines at the Advanced Photon Source. Images obtained at around 2 keV and 10 keV demonstrate the superiority of phase contrast over absorption for specimens composed of light elements.

Keywords: phase contrast; differential phase contrast; segmented detector; configured detector; fluorescence microprobe; X-ray microprobe; scanning microprobe.

1. Introduction

Scanning X-ray microprobes operating in the multi-keV region are excellent tools for the quantitative mapping of trace elements by X-ray fluorescence (XRF), often combined with X-ray absorption near-edge structure (XANES) measurements to provide localized information about chemical speciation (see *e.g.* Paunesku *et al.*, 2006; Fahrni, 2007). However, these techniques often do not image the ultrastructure of biological specimens well owing to the low photoelectric absorption and low fluorescent yield of light elements in this energy range. This can make it difficult to put trace elements into their structural context.

Phase contrast has received increased recognition as a complementary contrast mechanism in recent years (Momose, 2005). At lower photon energies, it can significantly reduce the radiation dose imposed on the specimen compared with absorption imaging (Schmahl *et al.*, 1994; Schneider, 1998). At higher energies, phase contrast dominates over absorption contrast particularly for light elements (see Fig. 1) and provides a means to image weakly absorbing specimens such as biological tissue.

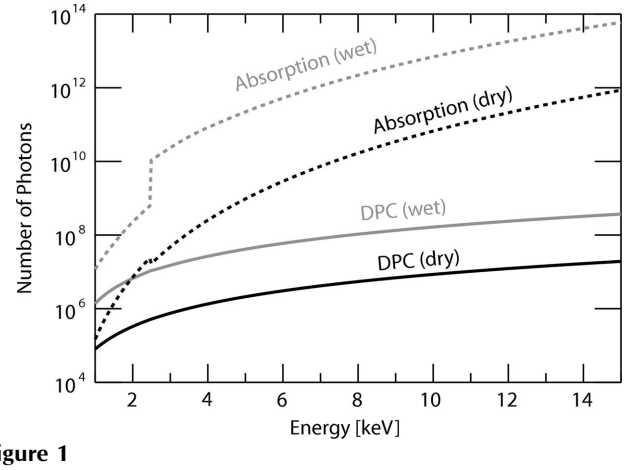

Figure 1
Number of photons required to see a 50 nm-thick protein structure in either air or 50 nm of water (Hornberger *et al.*, 2006). The calculation is based on a simple projection (for absorption) and refraction [for differential phase contrast (DPC)] model with photon statistics as the only noise source. It applies the Rose criterion of a minimum signal-to-noise ratio of five for the detectability of features (Rose, 1946). Atomic scattering data from Henke *et al.* (1993).

‡ Current address: Xradia Inc., 5052 Commercial Circle, Concord, CA 94520, USA.
¶ Current address: Australian Synchrotron, 800 Blackburn Road, Clayton, VIC 3168, Australia.

In an X-ray microprobe (which at lower photon energies is typically called a scanning transmission X-ray microscope, or STXM) an image is formed by raster-scanning the specimen through a focused X-ray beam (see Fig. 2). A fluorescence spectrum can be collected at each scan position using an energy-dispersive detector, and the total transmitted intensity and therefore specimen absorption is commonly measured with an area-integrating detector downstream of the specimen. Phase variations in the specimen do not affect the total transmitted intensity, but refract and diffract the beam, leading to a redistribution of intensity in the detector plane (for a mathematical description, see, for example, Hornberger *et al.*, 2007). This redistribution can be measured with an appropriately configured detector.

Table 1
Typical illumination conditions at the NSLS STXM (Feser *et al.*, 1998) and three different instruments at the APS: the 2-ID-B instrument (McNulty *et al.*, 2003), the 2-ID-E fluorescence microprobe and the Nanoprobe instrument currently under construction (Maser *et al.*, 2006).

Transmission imaging can be carried out very fast, while fluorescence measurements typically require longer pixel dwell times of the order of seconds.

Beamline	Primary application	Photon flux	Photon energy	Signal current	Dwell times
NSLS X1A	STXM	10^6 s^{-1}	200–800 eV	1–20 pA	1–10 ms
APS 2-ID-B	STXM/fluorescence	10^8 s^{-1}	1–4 keV	1–100 nA	ms–s
APS 2-ID-E	Fluorescence	10^9 s^{-1}	7–17 keV	0.1–1 µA	ms–s
APS Nanoprobe	Fluorescence	10^{10} s^{-1}	3–30 keV	0.5–5 µA	ms–s

The most flexible configuration is a fully pixelated detector such as a CCD (Chapman *et al.*, 1995; Gianoncelli *et al.*, 2006), whose response function can be modified arbitrarily in software after data acquisition. However, the pixel dwell time for transmission images in modern microprobes can be less than a millisecond; such short readout times are difficult to achieve with currently available pixel detectors. Moreover, to obtain a statistically meaningful signal in a large number of detector pixels a high dose to the specimen is required. Therefore, we have pursued the approach of a detector with fewer (eight to ten) segments, which has the advantages of fast readout (about 10 µs) and far reduced storage and data processing requirements compared with acquiring a full CCD frame at each image pixel. With such a detector, the difference signal of opposing segments provides differential phase contrast (Dekkers & Lang, 1974; Palmer & Morrison, 1991), which is a measure of the phase gradient of the specimen. The sum of all segments provides the same absorption signal as a single large-area detector. More elaborate analysis techniques allow the quantitative reconstruction of the specimen phase shift (see §3).

We have recently reported on the development of a segmented detector for use with a soft X-ray STXM at the National Synchrotron Light Source (NSLS) (Feser *et al.*, 2006). Now we describe the adaptation of that detector for use with harder X-rays at a third-generation synchrotron such as the Advanced Photon Source (APS). The detector consists of a segmented silicon photodiode chip and a set of charge integrating electronics, providing excellent performance even at the highest flux rates. The signal can be collected in parallel with the fluorescence spectrum for simultaneous absorption, phase and fluorescence imaging with intrinsic registration of all images. We present differential phase contrast examples which demonstrate greatly improved contrast over absorption imaging in the multi-keV range.

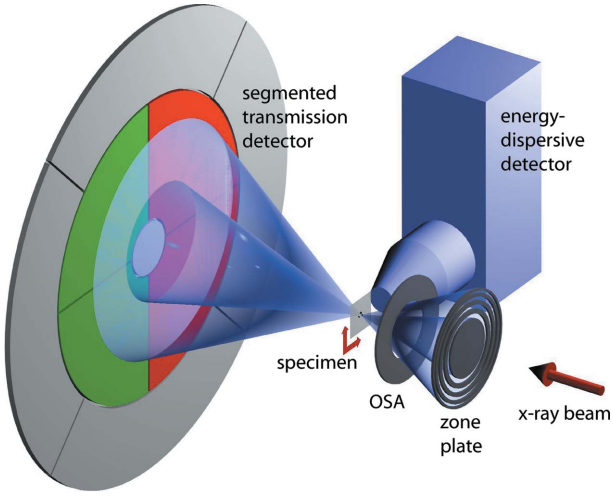

Figure 2
Schematic of a scanning X-ray microprobe. An optic, in our case a Fresnel zone plate (Michette, 1986), produces an X-ray focus, through which the specimen is raster-scanned. The image is acquired by recording the detector signal(s) at each scan position. The focal spot size, and therefore the spatial resolution, is roughly equal to the finest features of the zone plate. It is typically around 30–50 nm in the soft and intermediate X-ray range (up to a few keV), and around 100 nm for hard X-rays (around 10 keV). A combination of a central stop on the zone plate and an order-sorting aperture (OSA) is used to isolate the first-order focus of the zone plate, leading to a hollow-cone illumination of the specimen (Kirz *et al.*, 1995). Phase gradients in the specimen deflect the beam and lead to a redistribution of intensity on the transmission detector. In this illustration the difference signal between the green and red segments measures the horizontal beam shift. A single large-area transmission detector would only determine specimen absorption. A separate energy-dispersive detector measures fluorescence photons emitted by trace elements in the specimen.

2. Segmented charge-integrating silicon detector

Table 1 summarizes typical illumination conditions at several instruments. The requirements for the readout electronics are dictated by the signal current produced in the chip [see equation (1) below] and the desired pixel dwell time. It can be seen that the current at APS instruments is three or more orders of magnitude higher than at the NSLS, and that the pixel dwell times at the APS can vary over three orders of magnitude owing to slow fluorescence measurements. We have used a modified version of the soft X-ray detector for preliminary experiments at the APS (some examples are shown in §3.2), which was adequate for moderate signal levels. However, higher intensities required use of an aluminium absorber to avoid detector saturation (sometimes absorbing

more than 99% of the incident radiation); this absorber degrades the signal quality and is clearly very inefficient. In the following we describe the further development of the detector, in particular new electronics and a new readout mechanism, for the conditions present at the APS. For more details, see Hornberger (2007).

2.1. Segmented silicon chip

The detector chips are produced at the Max Planck Semiconductor Laboratory (MPI-HLL) in Munich, Germany, by the same technology used for the production of pn-CCDs for the X-ray multi-mirror satellite (XMM-Newton) (Strüder *et al.*, 2001). They are fabricated out of 300 to 450 µm-thick n-type high-resistivity (5 kΩ cm) silicon, commonly used for the detection of charged particles and X-rays. The back has a continuous n^+ implant which serves as an ohmic contact to apply a positive bias voltage. The front has all segments p-implanted with boron to form rectifying p/n junctions. The chip operates in direct-detection mode, without the use of a scintillator material. In the following we will focus on the behavior of the chip at higher photon energies; for more details see Feser *et al.* (2006). The different segmentations are discussed in §3.1.

2.1.1. Quantum efficiency. The quantum efficiency describes the fraction of photons absorbed in the depleted region of silicon. At photon energies above about 1 keV, where absorption in the surface oxide layer is negligible, the quantum efficiency can be approximated well by the chip thickness and the tabulated values of the X-ray absorption length if the chip is fully depleted with a sufficiently large reverse bias voltage. In this approximation, the quantum efficiency is almost 100% up to about 8 keV photon energy. At higher energies the efficiency drops owing to penetration through the silicon, falling to about 20% at 20 keV for a 300 µm-thick chip (see Fig. 3). Since the n-side entrance window is completely unstructured, the fill factor is 100% and does not influence the quantum efficiency.

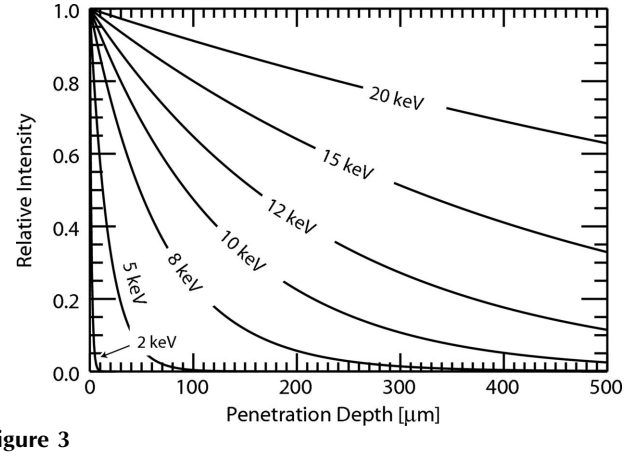

Figure 3
X-ray penetration into silicon for various photon energies. The quantum efficiency of the detector chip is given by the fraction of photons absorbed. A 300 µm-thick chip is almost 100% efficient up to 8 keV. Beyond that, the chip can still be used up to 15 or 20 keV with reduced efficiency. Data from Henke *et al.* (1993).

2.1.2. Illumination direction and radiation damage. As described by Feser *et al.* (2006), the front (segmented p-side) is sensitive to radiation damage, with the consequence that the leakage current increases considerably as the chip is exposed to X-rays. The back, however, has proved to be very radiation-hard with no increase in leakage current noticeable over years in soft X-ray experiments. In back illumination, the chip must be fully depleted even at lower photon energies where X-rays do not penetrate deep into the chip. This requires a bias voltage of about 100 V (depending on the wafer thickness and doping density), with leakage currents of the order of 2 pA per segment for the smaller segments.

At photon energies of about 10 keV and higher, radiation damage is a concern even in back-illumination, because a considerable fraction of photons penetrate through to the front side. At beamline 2-ID-E at the APS, we have noticed an increase in leakage current from about 2 pA per segment initially to about 15 pA after three days of regular use at 10 keV photon energy, and to about 700 pA after several months. However, this increase can be tolerated when signal currents exceed hundreds of nano-amperes (see Table 1). Radiation damage can be repaired by annealing the chip in a forming-gas atmosphere (a mixture of about 5% hydrogen in nitrogen) at 650 K for 1 h. To facilitate annealing, the chip has been mounted on a ceramic carrier that can easily be removed from the detector electronics box (see §2.4).

2.2. Charge integrating electronics

The readout electronics of the soft X-ray detector were optimized for low-noise integration of signal currents that were of the same order of magnitude as the detector leakage current (picoamperes). The required feedback capacitance of the integrator was of the same order of magnitude as the inherent capacitances of the components used (fractions of picofarads). The situation is inherently different for the beam parameters present at the APS, so that we have developed a completely new set of electronics. The new electronics are also optimized for shorter readout times and allow for the independent adjustment of signal current and integration time.

2.2.1. Operating principle. Fig. 4 shows a simplified schematic of one channel. A total of ten channels are available for readout of up to ten detector segments. The detector segment is depicted on the left as a reverse-biased diode (Det) producing a photocurrent. The resistor R_{cal} is added for

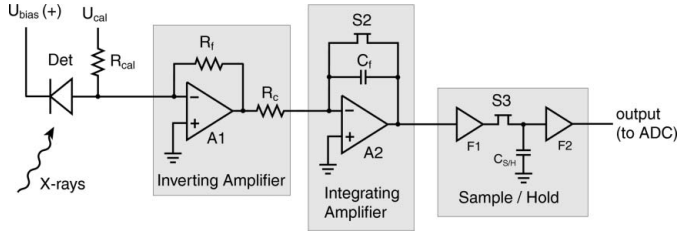

Figure 4
Simplified schematic of one channel of the charge integrating detector electronics (see text).

testing and calibration purposes. In the absence of a detector chip, a signal current can be emulated by applying a voltage U_{cal} to the calibration resistor.

The first stage is an inverting current amplifier (A1) which amplifies the photocurrent to a level within the design range of the second stage. The second stage is an integrating amplifier (A2) which collects the charge produced during one integration time (and amplified by A1) on the feedback capacitor C_f. The reset switch S2 is used to discharge the capacitor at the beginning of the integration cycle. At the end of the integration cycle, a sample-and-hold circuit (S/H) stores the integrator output for readout by an analog-to-digital converter (ADC), which is part of the microprobe data acquisition system. The S/H consists of two followers F1 and F2, a switch S3 and a capacitor $C_{S/H}$ (Horowitz & Hill, 1989).

2.2.2. Dynamic range. The division of the circuit into two independent amplifier stages allows for an independent adjustment to the photocurrent levels and desired integration times over a wide range of conditions. The input current I_{in} of the system is the photocurrent produced in the chip and is given by

$$I_{in} = \varepsilon e \Phi \frac{E}{3.62\,\text{eV}}, \quad (1)$$

where ε is the photon detection efficiency of the chip (see §2.1.1), e is the charge of the electron (1.602×10^{-19} C), Φ is the photon flux, E is the photon energy, and 3.62 eV is the energy required to produce one electron–hole pair in silicon at room temperature. The total gain of the system can be written as

$$U_{out} = \frac{R_f}{R_c C_f} I_{in} t_{int} \quad (2)$$

(Horowitz & Hill, 1989), where U_{out} is the output voltage of the integrator and t_{int} is the integration time. The feedback resistor R_f is chosen such that, for the maximum photocurrent expected in a detector segment (I_{max}), the first amplifier reaches the top of its output range (set to 5 V; $R_f = 5\ \text{V}/I_{max}$). The value of the feedback capacitor C_f of the integrator stage is set to 33 pF, which is an optimal value in terms of noise performance. The coupling resistor R_c can be adjusted so that the integrating amplifier reaches the top of its output range (again 5 V) at the longest desired integration time t_{max} ($R_c = t_{max}/33$ pF). Using the values in Table 1, it can be seen that R_f should be in the range of 3 MΩ, for high photon energy, high-flux applications, to 300 MΩ, for low photon energy, low-flux applications. R_c should be in the range of 10 MΩ, for 0.3 ms, to 100 MΩ, for 3 ms integration times.

2.2.3. Detector timing. Fig. 5 shows oscilloscope traces of a full integration cycle. A pulse (not shown, but see §2.2.4) triggers the start of a new cycle. The S/H circuit immediately switches to hold, storing the output voltage of the previous cycle for readout. With a short delay (1 µs), the reset switch S2 closes, discharging the feedback capacitor and bringing the output of the integrating amplifier to zero. Once the switch opens, the output of the integrator will rise linearly with the amount of charge delivered from the first amplifier stage.

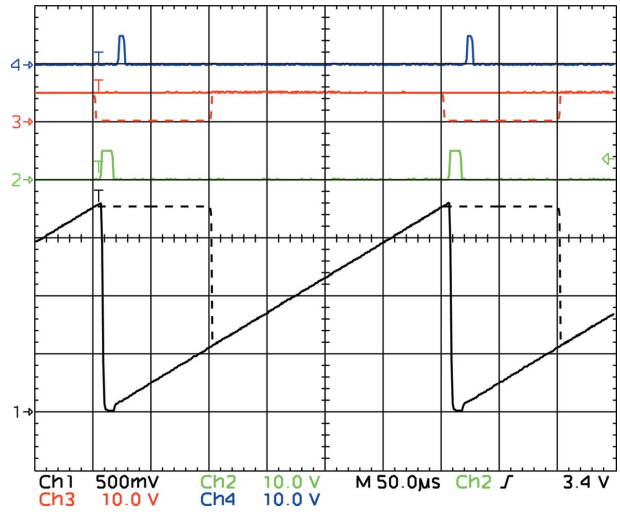

Figure 5
Full integration cycle of the detector electronics. Trace 1 shows the output of the sample-and-hold (S/H) circuit. Traces 2 and 3 show the control pulses of the reset and S/H switches, respectively. Trace 4 represents the acquisition pulse sent to the ADC. The solid lines show a cycle with the S/H disabled (following permanently), so that we directly see the output of the integrating amplifier. The dashed lines show a cycle with the S/H enabled. The small step in the integrator output at the end of the reset period is due to charge injection from the parasitic capacitance of the FET switch S2 into the feedback capacitor.

While the integration proceeds (and the S/H circuit is still on hold), an acquisition pulse is sent to an ADC (Acromag IP330; see http://www.acromag.com/) to read the voltage of the previous cycle from the S/H output. Once the readout is finished, S3 can switch to sampling (following) mode, until the next trigger pulse signals a new integration cycle. The control pulses are provided by a commercially available pulse generator (see §2.4).

The dead-time of the detector is given by the width of the reset pulse plus its delay from the closing of the S/H switch. The decay time for the discharge of C_f is a few hundreds of nanoseconds, so that the dead-time can be as low as a few microseconds. This allows for pixel dwell times below 100 µs.

2.2.4. Interfacing with microscope electronics. Scanning X-ray microprobes can usually operate in either step- or fly-scan mode. In step-scan mode the sample is moved in discrete steps and stays at each scan position for a fixed dwell time. In fly scan mode the scanning stage moves continuously for each scan line, and a trigger signal at constant spatial intervals is generated to define the pixels. The pixel size and the desired pixel dwell time dictate the motor speed required, and the actual dwell time per pixel can be measured using a clock signal.

The integrating circuit is designed for continuous operation: an incoming trigger simultaneously signals the end of one integration cycle and the beginning of the next one. This matches well with the fly-scan mode of the microprobe, where a pixel-advance trigger can signal the separation between integration cycles. At the beginning of the integration cycle, the signal of the previous cycle is made available for readout on the S/H circuit (without disturbing the ongoing cycle).

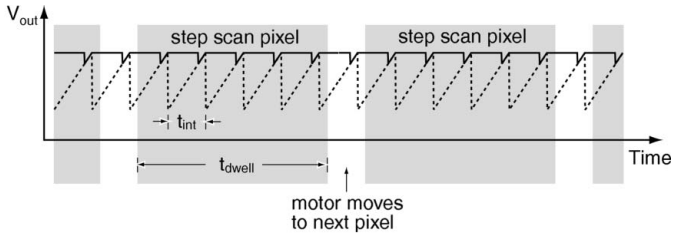

Figure 6
Detector readout scheme in step-scan mode. The dashed line shows schematically the output voltage of the integrating amplifier with periodic reset. The output of the sample-and-hold circuit (solid line) is 'quasi-constant' owing to the S/H being set to hold for most of the integration time. The pixel dwell time t_{dwell}, indicated by the gray boxes, is much longer than the detector integration time t_{int}. The short sampling period of the S/H circuit (about 20 µs) introduces a negligible inaccuracy.

Step-scan mode is often slow owing to the overhead of addressing, accelerating and decelerating a motor and is normally used for long dwell times of about 0.1 s up to several seconds (*e.g.* for fluorescence measurements). The electronics cannot accommodate such long integration times while at the same time delivering low-noise performance at millisecond dwell times in fly-scan mode and being able to accommodate variations in photon flux over a few orders of magnitude. Therefore we have developed a scheme to operate the detector in a quasi-current mode which decouples the detector integration time from the pixel dwell time.

This is illustrated in Fig. 6. The detector timing module provides a constant-frequency reset trigger (fast enough to avoid saturation of the integrator and much faster than the typical pixel rate of step scans), which does not have to be synchronized with the scanning process. The S/H circuit is set to hold for most of the integration period so that the output provides a 'quasi-constant' voltage representing a real-time measure of photon rate. Instead of using an ADC, the voltage is fed into a voltage-to-frequency converter (Nova N101VTF; see http://www.novarad.com/). The total number of pulses during the pixel dwell time is a measure of the average detector output voltage within that period.

2.2.5. Linearity, noise and relative dynamic range. We have measured the output voltage of the circuit for variable integration times with a constant input voltage applied to the calibration resistor, and for variable input voltages and constant integration time. In each case a linear fit can determine the calibration constant α that describes the gain of the circuit (see §2.3.2). The result is shown in Fig. 7. In both cases the residuals between data and fit indicate a slight non-linearity. However, the standard deviations of the residuals are only 0.89 mV (for variable integration time) and 1.3 mV (for variable input voltage), compared with a noise level of about 1 mV (see below), and the effect was not investigated further.

The variations of the output voltage were less than 1 mV and about the same as the variations measured in the calibration input voltage. Therefore the integrating electronics did not introduce any noise above the sensitivity of the set-up used for the measurement. With an amplifier range of 5 V, the dynamic range is better than 5000.

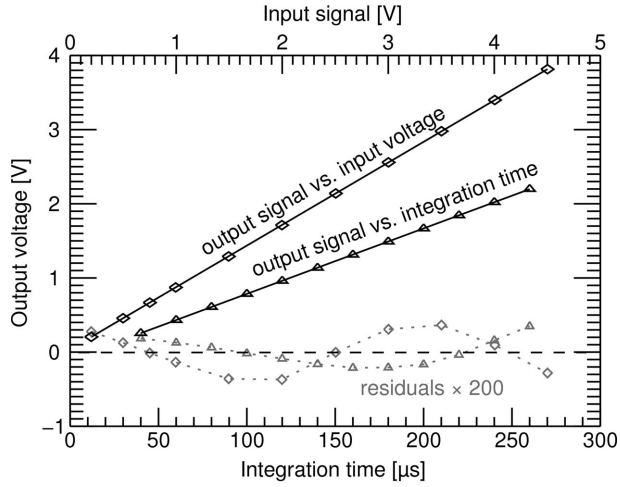

Figure 7
Linearity of the electronics with integration time (bottom axis) and with input signal (top axis). In both cases the error bars are too small to display. The residuals (increased by a factor of 200 in the plot) indicate a slight non-linearity.

2.3. Detector calibration

The detector can be absolutely calibrated in terms of X-ray flux. The procedure is very similar to the first version of the detector (Feser *et al.*, 2006), so that we only summarize the important results here.

2.3.1. Channel crosstalk. Owing to capacitive coupling of the preamplifier inputs and outputs of different channels (mainly determined by the proximity of the amplifiers and conductive lines on the printed-circuit boards), a signal in one electronics channel can induce a (much smaller) signal in one or more other channels. The crosstalk can be measured and corrected for in software after data acquisition. In practice, the crosstalk coefficients are of the order of 10^{-4} or smaller.

2.3.2. Voltage to photon flux conversion. After the crosstalk correction, the photon flux Φ can be determined from the measured output voltage of the S/H circuit U_{SH} by (Feser *et al.*, 2006)

$$\Phi = \frac{U_{SH} - U_0 - \alpha I_{dark} t_{int}}{\alpha q (t_{int} - t_{dead})}, \qquad (3)$$

where U_0 is the output voltage extrapolated to zero integration time, α is a calibration constant describing the output voltage rise per input charge injected into the system, I_{dark} is the dark (leakage) current of the system, q is the average charge deposited in the detector chip per incident X-ray photon, t_{int} is the duration of the integration cycle and t_{dead} is the dead time. U_0 and the product αI_{dark} can be determined by measuring the output voltage in dark conditions (no X-rays incident) for a range of integration times and applying a linear fit. The constant α is given by the values of the feedback and coupling resistors and the feedback capacitor; it can be determined more accurately by applying a voltage to the known calibration resistor and measuring the slope of the output voltage *versus* integration time (see §2.2.5). The parameter q contains the photon detection efficiency of the chip

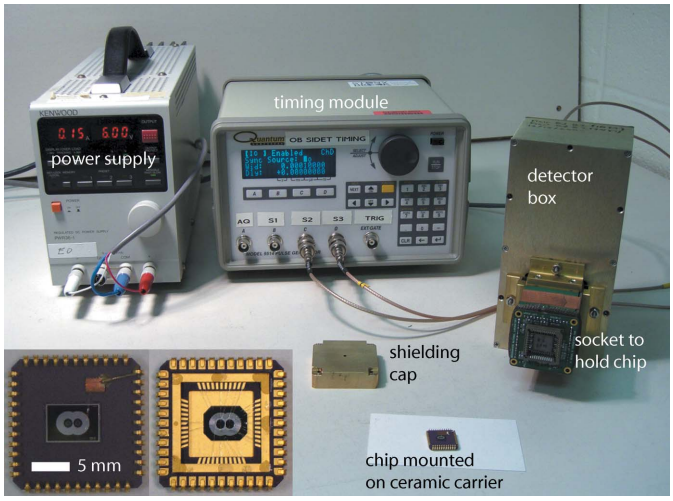

Figure 8
Hardware components of the detector. The insets show the chip mounted on a ceramic carrier. Each chip has two segment structures, only one of which is used at a time (Feser *et al.*, 2006). Left inset: back (n-) of the chip. This is the side where the X-rays will be incident. A wire connection on the upper right carries the bias voltage. Right inset: segmented front (p-) side. Wire bonds connect the detector segments to the carrier pins through a cut-out in the carrier.

and the statistics of photon to charge conversion in silicon; therefore it depends on the photon energy.

2.4. Detector components

Fig. 8 shows a photograph of the detector components. The chip is mounted on a ceramic carrier which is inserted into a socket in the detector snout and can easily be exchanged or removed for annealing. A custom-made housing holds the printed-circuit boards as well as a stack of watch batteries, which provides the bias voltage for the chip. A commercially available timing module (Quantum Composers Model 9514 Option 403) provides the control pulses for the switches as well as the acquisition pulse sent to the ADC. It can be triggered externally for integration in sync with the scanning process, or can generate its own reset trigger. A power supply (Kenwood PW36-1.5AD) provides stable ± 6 V supply voltages for the components of the circuit.

3. Detector segmentation and imaging modes

3.1. Configuration of segments

Several criteria determine the best choice of segmentation. A simple quadrant structure is easy to align and provides differential phase contrast in two orthogonal directions with the potential for phase reconstruction by integration (see below). A finer segmentation in the radial and/or angular directions provides better theoretical performance in terms of contrast transfer functions (Hornberger, 2007, §4.2.5), but is more difficult to align and interpret, particularly if the illumination is not completely uniform. An outer annular segment, which is not directly illuminated by the incident X-ray beam, can be used for dark-field imaging (Morrison & Browne, 1992; Chapman *et al.*, 1996) if the sensitivity of the corresponding read-out channel is sufficient to detect the weak signal levels of the radiation scattered outside of the bright-field cone. A small central segment is useful for alignment purposes and to mask out radiation leaking through or around the central stop of a zone plate (see Fig. 2). Except for dark-field contrast, it does not contribute significantly to the actual imaging process, because it lies in the shadow of the central stop and therefore does not receive any focused first-order radiation.

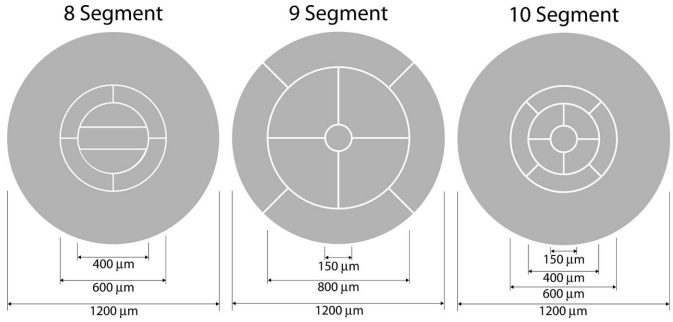

Figure 9
Available segmentations of the detector chip (see text).

The currently available segmentations of the detector chip are shown in Fig. 9. The eight-segment structure was originally designed to also enable a Nomarski interference contrast mode (Polack *et al.*, 1998) which requires the parallel segments in the center. The nine-segment structure proved most useful in recent experiments, because with proper alignment (keeping the beam on the inner part of the chip) it is equivalent to a simple quadrant structure. The ten-segment structure provides better contrast transfer functions for the same beam coverage, but is more sensitive to non-uniformities in the beam and does not allow phase reconstruction by direct integration (see below).

These segmentations were designed for beam diameters of about 600 µm, which is a practical size for common instrument dimensions. With typical zone-plate diameters of about 150 µm, this means that the detector is positioned a few focal lengths downstream of the specimen. The detector is mounted on a motorized XYZ platform which allows for position adjustment according to the zone plate and X-ray energy used, as well as transverse alignment to the X-ray beam.

3.2. Differential phase contrast

Differential phase contrast (DPC) images are readily obtained from the difference signal of opposing segments and can be displayed in real time. Therefore it is very useful for rapid specimen overview and feature recognition. This section provides a few examples to illustrate the striking differences between absorption and DPC at higher X-ray energies. At 10 keV photon energy, the difference is dramatic, as illustrated in images of 5 µm polystyrene spheres (Fig. 10), phytoplankton cells (Fig. 11) and a cardiac myocyte (heart muscle cell; Fig. 12). At energies around 2 keV, absorption contrast increases but phase contrast is still superior, as shown in

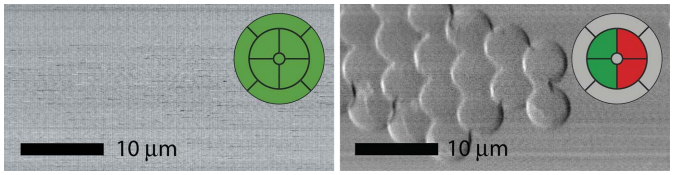

Figure 10
Absorption (left) and DPC (right) images of 5 µm-diameter polystyrene spheres recorded at 10 keV photon energy at beamline 2-ID-E at the APS. Both images are generated from the same data set, using different combinations of detector segments as indicated by the insets (see Fig. 9; green, added; red, subtracted; gray, not used). The spheres are completely invisible in absorption contrast, but well visible in DPC. We have used a zone plate with an outermost zone width of 100 nm, a step size of 50 nm and a pixel dwell time of 3 ms.

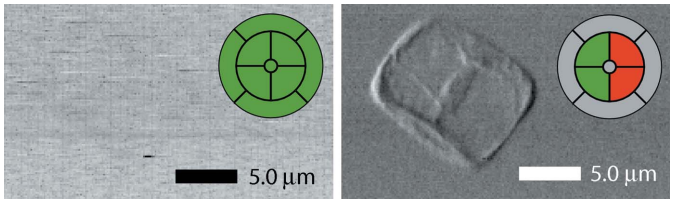

Figure 11
Absorption (left) and DPC (right) images of a diatom (phytoplankton cell) recorded at 10 keV photon energy at beamline 2-ID-E. As above, the specimen is completely invisible in absorption, but clearly visible in phase contrast. We have used the same 100 nm-outermost-zone-width zone plate as above, a step size of 100 nm and a pixel dwell time of 2 ms. Sample courtesy of Ben Twining and Stephen Baines (Marine Sciences Research Center, Stony Brook University).

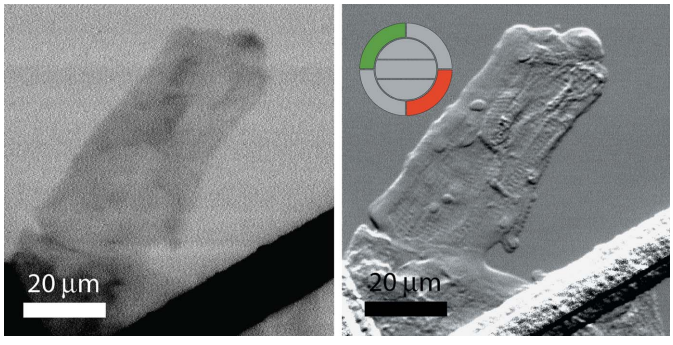

Figure 12
Absorption (left) and DPC (right) images of a freeze-dried cardiac myocyte recorded at 10 keV photon energy at 2-ID-E. While the specimen is relatively thick and therefore visible in absorption contrast (here recorded with an ion chamber rather than the segmented detector), the phase-contrast image shows considerably more detail, in particular the cross-striations typical of heart muscle. Sample provided by B. M. Palmer, University of Vermont. Image recorded with the modified soft X-ray detector and an aluminium absorber. The step size is 200 nm, and the dwell time is 10 ms.

images of a diatom (Fig. 13) and 5 µm polystyrene spheres (Fig. 14).

3.3. Quantitative phase reconstruction

DPC images can be difficult to interpret owing to the differential nature and the directional dependence of the signal (Morrison & Chapman, 1983), so that a map of the

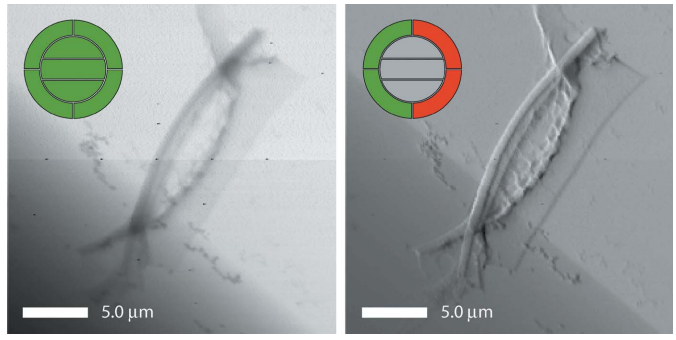

Figure 13
Absorption (left) and DPC (right) images of a diatom (phytoplankton cell) recorded at 1790 eV photon energy at beamline 2-ID-B at the APS. This image was also obtained with the modified soft X-ray detector. While the specimen is visible in absorption, the DPC image shows considerably more detail. The diagonal line visible in both images is the edge of a silicon nitride window. The horizontal line is caused by a sudden change in X-ray intensity; thus it is almost invisible in the differential measurement. This image was recorded using a 50 nm-outermost-zone-width zone plate, 25 nm steps and 3 ms dwell time.

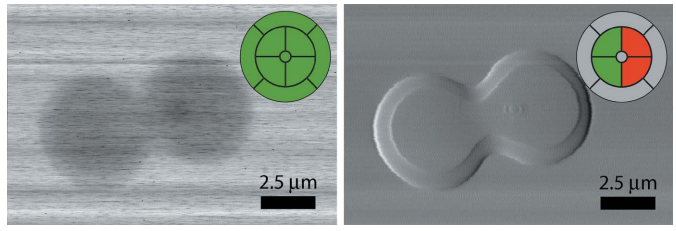

Figure 14
Absorption (left) and DPC (right) images of 5 µm-diameter polystyrene spheres recorded at 2500 eV photon energy at beamline 2-ID-B. At this photon energy the spheres are visible in absorption, but show much more detail in DPC. The pedestal around the spheres is due to residual solution, and the small bump on the right-hand sphere is due to radiation damage caused by a 30 s exposure to the focused X-ray beam. This scan was performed with a 50 nm-outermost-zone-width zone plate, 25 nm steps and 5 ms dwell time.

absolute phase shift is preferred. Furthermore, if the composition of the specimen is known or can be estimated, tabulated values of the refractive index (Henke *et al.*, 1993) can be used to derive the mass or thickness from the absolute phase shift. In combination with fluorescence measurements, this allows the calculation of trace-element concentrations rather than absolute amounts to greatly improve the interpretation of fluorescence data sets.

Currently, we are implementing two different methods for the reconstruction of the absolute phase shift from segmented detector data. The method of Fourier filtering (Hornberger *et al.*, 2007), based on McCallum *et al.* (1995, 1996), is an inversion of the imaging process by 'deconvolving' the contrast transfer functions (similar to the Wiener filter) and requires a weak specimen approximation. Alternatively, the horizontal and vertical DPC images can be interpreted as two orthogonal gradient maps which can be integrated with a Fourier derivative method (de Jonge *et al.*, 2007, 2008), based on Arnison *et al.* (2004) and Kottler *et al.* (2007). While this technique

assumes a constant phase gradient across the width of the probe, it has the advantage that more strongly absorbing and phase shifting specimens can be reconstructed.

4. Conclusions

We have reported on the development of a segmented detector for combined amplitude and phase-contrast imaging in scanning X-ray microprobes at modern third-generation synchrotron sources. The detector can be operated over a wide range of conditions and is currently installed at beamlines 2-ID-B and 2-ID-E at the APS. Installations at further beamlines are planned in the near future. Fast readout allows for short pixel dwell times in transmission imaging, to make full use of the high brightness provided by current undulator beamlines. The silicon detector chip has very good quantum efficiency up to about 12 keV, compatible with the X-ray energy range most commonly used for fluorescence imaging.

We have provided examples to demonstrate the superiority of phase over absorption contrast for biological specimens in the multi-keV range. When fluorescence is used for trace-element mapping, phase contrast can simultaneously provide good quality images of the underlying tissue. We have indicated two techniques for quantitative phase recovery, which can be used to infer the specimen thickness to turn trace element amounts into concentrations. DPC has also proved extremely valuable for fast overview scans to locate interesting sample regions in preparation for long fluorescence measurements.

Work at Stony Brook University was supported by the National Science Foundation under contract CHE-0221934. Work at the Brookhaven National Laboratory Instrumentation Division was supported by the US Department of Energy, Office of Science, Office of Basic Energy Sciences, under Contract No. DE-AC02-98CH10886. Use of the Advanced Photon Source was supported by the US Department of Energy, Office of Science, Office of Basic Energy Sciences, under Contract No. DE-AC02-06CH11357. Work at the Max Planck Semiconductor Laboratory was supported by the Max Planck Society.

References

Arnison, M. R., Larkin, K. G., Sheppard, C. J. R., Smith, N. I. & Cogswell, C. J. (2004). *J. Microsc.* **214**, 7–12.
Chapman, H. N., Jacobsen, C. & Williams, S. (1995). *Rev. Sci. Instrum.* **66**, 1332–1334.
Chapman, H. N., Jacobsen, C. & Williams, S. (1996). *Ultramicroscopy*, **62**, 191–213.
Dekkers, N. H. & de Lang, H. (1974). *Optik*, **41**, 452–456.
Fahrni, C. J. (2007). *Curr. Opin. Chem. Biol.* **11**, 121–127.
Feser, M., Carlucci-Dayton, M., Jacobsen, C. J., Kirz, J., Neuhäusler, U., Smith, G. & Yu, B. (1998). *Proc. SPIE*, **3449**, 19–29.
Feser, M., Hornberger, B., Jacobsen, C., De Geronimo, G., Rehak, P., Holl, P. & Strüder, L. (2006). *Nucl. Instrum. Methods Phys. Res. A*, **565**, 841–854.
Gianoncelli, A., Morrison, G. R., Kaulich, B., Bacescu, D. & Kovac, J. (2006). *Appl. Phys. Lett.* **89**, 251117.
Henke, B. L., Gullikson, E. M. & Davis, J. C. (1993). *Atom. Data Nucl. Data Tables*, **54**, 181–342.
Hornberger, B. (2007). PhD thesis, Stony Brook University, USA.
Hornberger, B., Feser, M. & Jacobsen, C. (2007). *Ultramicroscopy*, **107**, 644–655.
Hornberger, B., Feser, M., Jacobsen, C., Vogt, S., Legnini, D., Paterson, D., Rehak, P., De Geronimo, G. & Palmer, B. M. (2006). *X-ray Microscopy: Proceedings of the 8th International Conference, IPAP Conference Series*, edited by S. Aoki, Y. Kagoshima and Y. Suzuki, pp. 396–398. Tokyo: Institute of Pure and Applied Physics.
Horowitz, P. & Hill, W. (1989). *The Art of Electronics*, 2nd ed. Cambridge University Press.
Jonge, M. D. de, Hornberger, B., Holzner, C., Legnini, D., Paterson, D., McNulty, I., Jacobsen, C. & Vogt, S. (2008). *Phys. Rev. Lett.* **100**, 163902.
Jonge, M. D. de, Vogt, S., Legnini, D., McNulty, I., Rau, C., Paterson, D., Hornberger, B., Holzner, C. & Jacobsen, C. (2007). *Nucl. Instrum. Methods Phys. Res. A*, **582**, 218–220.
Kirz, J., Jacobsen, C. & Howells, M. (1995). *Q. Rev. Biophys.* **28**, 33–130. [Also available as Lawrence Berkeley National Laboratory report LBL-36371, LBNL, CA, USA.]
Kottler, C., David, C., Pfeiffer, F. & Bunk, O. (2007). *Opt. Express*, **15**, 1175–1181.
McCallum, B. C., Landauer, M. N. & Rodenburg, J. M. (1995). *Optik*, **101**, 53–62.
McCallum, B. C., Landauer, M. N. & Rodenburg, J. M. (1996). *Optik*, **103**, 131–132.
McNulty, I., Paterson, D., Arko, J., Erdmann, M., Frigo, S. P., Goetze, K., Ilinski, P., Krapf, N., Mooney, T., Retch, C. C., Stampfl, A. P. J., Vogt, S., Wang, Y. & Xu, S. (2003). *J. Phys. IV*, **104**, 11–15.
Maser, J. *et al.* (2006). *X-ray Microscopy: Proceedings of the 8th International Conference, IPAP Conference Series*, edited by S. Aoki, Y. Kagoshima and Y. Suzuki, pp. 26–29. Tokyo: Institute of Pure and Applied Physics.
Michette, A. G. (1986). *Optical Systems for Soft X-rays.* New York: Plenum.
Momose, A. (2005). *Jpn. J. Appl. Phys.* **44**, 6355–6367.
Morrison, G. R. & Browne, M. T. (1992). *Rev. Sci. Instrum.* **63**, 611–614.
Morrison, G. R. & Chapman, J. N. (1983). *Optik*, **64**, 1–12.
Palmer, J. R. & Morrison, G. R. (1991). *OSA Proceedings on Short Wavelength Coherent Radiation: Generation and Applications*, edited by P. H. Bucksbaum & N. M. Ceglio, Vol. 11, pp. 141–145. Washington: Optical Society of America.
Paunesku, T., Vogt, S., Maser, J., Lai, B. & Woloschak, G. (2006). *J. Cell. Biochem.* **99**, 1489–1502.
Polack, F., Joyeux, D. & Phalippou, D. (1998). *X-ray Microscopy and Spectromicroscopy*, edited by J. Thieme, G. Schmahl, E. Umbach and D. Rudolph, pp. I105–I109. Berlin: Springer-Verlag.
Rose, A. (1946). *J. Soc. Motion Picture Eng.* **47**, 273–294.
Schmahl, G., Rudolph, D., Schneider, G., Guttmann, P. & Niemann, B. (1994). *Optik*, **97**, 181–182.
Schneider, G. (1998). *Ultramicroscopy*, **75**, 85–104.
Strüder, L. *et al.* (2001). *Astron. Astrophys.* **365**, L18–L26.